JBC RESEARCH ARTICLE

The coiled-coil domain of *Escherichia coli* FtsLB is a structurally detuned element critical for modulating its activation in bacterial cell division

Received for publication, August 25, 2021, and in revised form, November 24, 2021 Published, Papers in Press, December 4, 2021,
https://doi.org/10.1016/j.jbc.2021.101460

Samuel J. Craven[1,2], **Samson G. F. Condon**[1,2], **Gladys Díaz Vázquez**[1,3], **Qiang Cui**[4], **and Alessandro Senes**[1,*]

From the [1]*Department of Biochemistry,* [2]*Integrated Program in Biochemistry, and* [3]*Biophysics Graduate Program, University of Wisconsin-Madison, Madison, Wisconsin, USA;* [4]*Department of Chemistry, Boston University, Boston, Massachusetts, USA*

Edited by Chris Whitfield

The FtsLB complex is a key regulator of bacterial cell division, existing in either an *off* state or an *on* state, which supports the activation of septal peptidoglycan synthesis. In *Escherichia coli*, residues known to be critical for this activation are located in a region near the C-terminal end of the periplasmic coiled-coil domain of FtsLB, raising questions about the precise role of this conserved domain in the activation mechanism. Here, we investigate an unusual cluster of polar amino acids found within the core of the FtsLB coiled coil. We hypothesized that these amino acids likely reduce the structural stability of the domain and thus may be important for governing conformational changes. We found that mutating these positions to hydrophobic residues increased the thermal stability of FtsLB but caused cell division defects, suggesting that the coiled-coil domain is a "detuned" structural element. In addition, we identified suppressor mutations within the polar cluster, indicating that the precise identity of the polar amino acids is important for fine-tuning the structural balance between the *off* and *on* states. We propose a revised structural model of the tetrameric FtsLB (named the "Y-model") in which the periplasmic domain splits into a pair of coiled-coil branches. In this configuration, the hydrophilic terminal moieties of the polar amino acids remain more favorably exposed to water than in the original four-helix bundle model ("I-model"). We propose that a shift in this architecture, dependent on its marginal stability, is involved in activating the FtsLB complex and triggering septal cell wall reconstruction.

Cell division in bacteria is a complex process involving intricate coordination between numerous cellular components. Central to this coordination is the divisome, a multiprotein complex that in the Gram-negative bacterium *Escherichia coli* consists of a number of essential proteins (FtsZ, FtsA, ZipA, FtsE, FtsX, FtsK, FtsQ, FtsL, FtsB, FtsW, FtsI, and FtsN; Fig. 1) as well as a suite of nonessential, conditionally essential, and redundant proteins (1, 2). These proteins mediate the various functions necessary for cell division, including establishing the site of division, coordinating invagination of the inner and outer membranes, and remodeling the cell wall at midcell into a septum to compartmentalize the nascent daughter cells. If any of these functions is abrogated through deletion or mutation of essential proteins, the bacteria can continue to elongate and replicate their DNA, but they will be unable to divide and form distinct daughter cells. This will result in the formation of long filaments and eventual cell lysis and death.

Remodeling of the cell wall during division involves degradation of old peptidoglycan (PG) at the division site and synthesis of new material, leading to the formation of a septum that eventually splits into the poles of the nascent daughter cells. Numerous nonessential and redundant enzymes (*e.g.*, periplasmic hydrolases) participate in PG reconstruction (3–5), but the major synthetic activity is performed by the essential FtsWI complex (6–8). FtsW—a large multipass membrane protein—is a PG glycosyltransferase that polymerizes novel glycan strands from lipid II precursors (9, 10) (FtsW was also previously reported to have lipid II flippase activity (11–13)). FtsI is the cognate transpeptidase of FtsW and is responsible for crosslinking the glycan polymers to form a network of PG strands (6, 14). Forming the septum requires other PG synthases (*e.g.*, either of the bifunctional glycosyltransferase/transpeptidases PBP1a or PBP1b (15)), but functional redundancy between these proteins means that no individual component is essential apart from FtsWI.

The mere presence of FtsWI at midcell is not, however, sufficient for completion of cytokinesis. Instead, the complex must be switched on, and this activation (along with the consequent triggering of cell wall reconstruction) is a tightly regulated step of cell division (1, 16, 17). In current models, activation begins with the midcell localization of FtsN (18–20) (Fig. 1*C*), which communicates with FtsWI through a cytoplasmic route involving FtsA (21–23) and through a periplasmic route involving the FtsLB complex (21, 24–27). In this work, we focus on the latter periplasmic activation route.

FtsL and FtsB are both single-pass membrane proteins with a short (FtsL) or minimal (FtsB) N-terminal tail in the cytoplasm and a larger C-terminal domain in the periplasm. They form a heterotetrameric complex consisting of two FtsL and two FtsB subunits arranged into a long helical bundle formed

* For correspondence: Alessandro Senes, senes@wisc.edu.

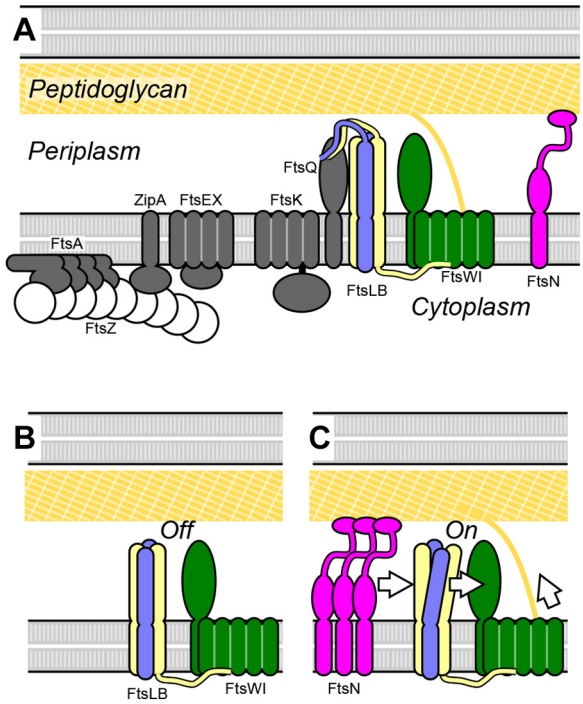

Figure 1. The current model for activation of cell division. *A,* schematic representation of the essential components of the *Escherichia coli* divisome. The polymeric ring formed by FtsZ establishes the site of division in coordination with other early components. The peptidoglycan synthase complex FtsWI is the main actor for the reconstruction of the cell wall, leading to the formation of a septum and, eventually, the poles of the nascent daughter cells. Its activation is tightly regulated by FtsN and FtsLB. *B,* in the current model, FtsWI is in complex with FtsLB but is initially inactive. *C,* accumulation of FtsN at midcell somehow triggers a conformational change in the FtsLB complex, which in turn triggers peptidoglycan synthesis likely by a direct interaction with FtsWI.

by its transmembrane and periplasmic coiled-coil domains (28, 29) (Fig. 2*A*). The N-terminal cytoplasmic tail of FtsL is involved with recruiting FtsWI to the division site, whereas the C-terminal periplasmic tail of FtsB binds with high affinity to another divisome protein FtsQ and is needed for recruitment of FtsLB to midcell (30–35). The structure of FtsLB has not been solved experimentally aside from fragments (34–36), but computational structural models of its helical bundle region are available. Originally, the Monasterio group proposed models of the soluble coiled-coil region in complex with the periplasmic domain of FtsQ, in either trimeric or hexameric configurations (37). More recently, using a set of amino acid contacts postulated by evolutionary coupling, we derived a model that includes both the transmembrane region and the coiled coil (29). In this model, the transmembrane and coiled-coil domains of FtsL form a continuous helix, whereas FtsB contains a potentially flexible Gly-rich linker that breaks the helix between these two regions (36).

In current models, FtsLB regulates FtsWI septal PG synthesis activity by transitioning from an *off* state to an *on* state in response to a signal from FtsN (Fig. 1*C*). This idea was initially proposed following the identification of a series of gain-of-function mutations within both FtsL and FtsB that enable survival in the absence of the normally essential FtsN (21, 24). Along with subsequent work (25, 26), this led to the identification of two related regions at the C-terminal end of the FtsLB coiled coil that are central to its regulation of FtsWI. The first region, named the constriction control domain (CCD; approximately residues 88–94 in FtsL and 55–59 in FtsB), houses the aforementioned *ΔftsN*-suppressing mutations (21, 24). The second region neighbors the CCD on the opposite helical face of FtsL specifically and is designated as activation of FtsWI (AWI; positions 82–84, 86–87, and 90). Dominant-negative mutations in FtsL indicate that the AWI region directly interacts with and activates FtsWI (25, 26), suggesting that the *off/on* transition in FtsLB may involve conformational changes that make the AWI region available to interact with and activate FtsWI. Normally, either direct or indirect interactions with FtsN are required to trigger such a change; however, the gain-of-function CCD mutations may induce similar structural rearrangements of FtsLB, thereby mimicking the signal from FtsN and bypassing its requirement to trigger septal PG reconstruction. Whatever conformational changes in FtsLB are required for this activation, they will likely depend on the extended helical topology that is at the core of the complex (29, 32, 38, 39).

One intriguing structural feature of FtsLB is the unusual presence of a cluster of strongly polar amino acids buried at interfacial positions of the coiled coil (*i.e.*, at positions designated as "*a*" and "*d*" in the "*abcdefg*" heptad repeat). This "polar cluster" (as it will be referred to from now on) consists of two arginine residues (R67 and R74) in FtsL and of a glutamine residue (Q39) and two asparagine residues (N43 and N50) in FtsB (Fig. 2*B*). Since canonical coiled coils contain primarily hydrophobic residues at the interfacial "*a*" and "*d*" positions (40), the polar cluster is likely to decrease the stability of the coiled coil (29). This suggests that these nonideal residues play some critical role in modulating the stability and dynamics of the FtsLB complex, which likely has important functional consequences—a hypothesis that we address in this present article.

We hypothesize that the coiled coil of FtsLB is detuned for stability in order to support the dynamics necessary for structural transitions that occur during the *off* to *on* switch at the heart of FtsWI regulation. Here, we show that hydrophobic mutations introduced in the polar cluster of FtsLB stabilize the coil but lead to cell division defects *in vivo*. We also show that the identity of the interfacial residues is important for the observed division phenotypes, indicating those residues may play a more nuanced role than simply destabilizing the hydrophobic coiled-coil interface and are likely to participate in the balance of forces that regulate the *off/on* transition of the complex. In addition, because the presence of polar residues at "*a*" and "*d*" positions statistically favors the formation of two-stranded coiled coils (41–43), we investigated an alternative model of FtsLB in which the coiled-coil region splits into a pair of two-stranded coiled-coil domains (the Y-model), as opposed to the monolithic four-stranded coil that we originally proposed (29) (the I-model). This revised model fits the available evidence as well as the original I-model, while displaying better behavior, and thus,

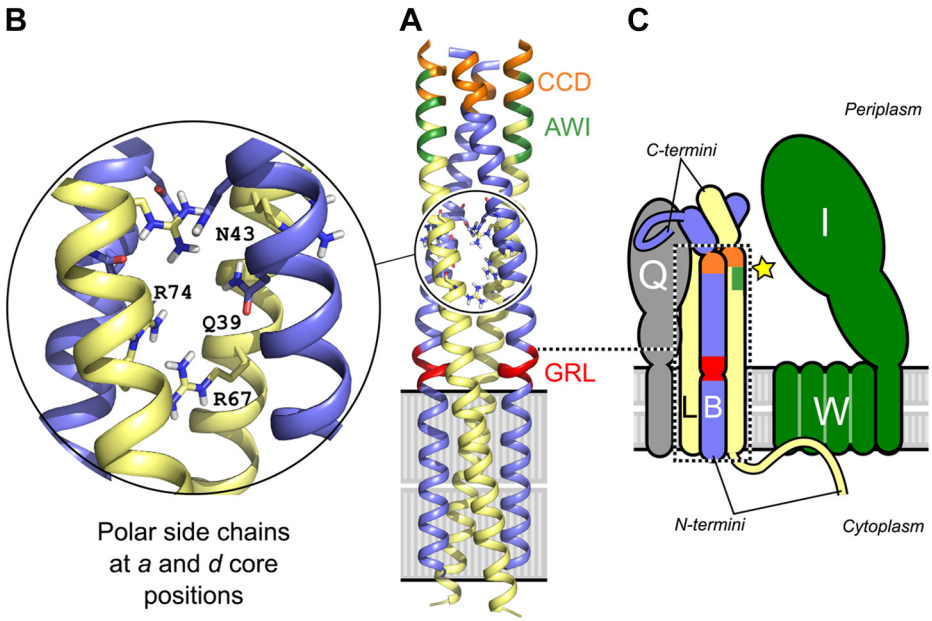

Figure 2. An unusual cluster of strong polar amino acids in the core of the computational model (I-model) of FtsLB likely tunes its stability and conformation dynamics. *A,* original computational model of the tetrameric helical bundle of FtsLB (29), referred to here as the I-model. The model is formed by two FtsL (*yellow*) and two FtsB (*blue*) units. FtsL forms a continuous helix across the membrane and periplasmic domains, whereas the helix of FtsB is interrupted in the juxtamembrane region by an unwound Gly-rich linker (GRL, *red*). Highlighted in *orange* and *green* are the CCD and AWI regions, respectively, which occur near a predicted hinge at the C-terminal end of the coiled coil. These regions are critical for FtsLB activation. *B,* the coiled coil contains a cluster of polar amino acids at core "*a*" and "*d*" positions, including two Arg residues in FtsL (positions 67 and 74) and Gln-39 and Asn-43 in FtsB. The polar cluster is likely to be a destabilizing feature of the coiled coil. *C,* schematic representation of FtsLB and its interactions with FtsQ and the FtsWI complex. The region corresponding to the model is enclosed in the *dotted box*. The interaction with FtsQ is largely mediated by the C-terminal tail of FtsB. The interaction with FtsW is mediated by the N-terminal tail of FtsL. The star indicates the putative activating contact between the AWI region of FtsL and FtsI. AWI, activation of FtsWI; CCD, constriction control domain.

we propose it as the more likely candidate for the structural organization of FtsLB.

Results and discussion

The polar cluster of FtsLB is an unusual feature for coiled-coil structures

Although "*a*" and "*d*" positions of coiled coils tend to be mainly hydrophobic, polar amino acids can also occur there. To determine if the coiled coil of FtsLB is unusually rich in interfacial polar amino acids in comparison with other coiled coils, we performed a structural analysis of the 2662 crystal structures available in the CC+ database (44). We found that polar amino acids, such as Asp, Glu, His, Arg, Lys, Gln, and Asn, occur with a frequency of 17.6% at "*a*" or "*d*" positions, corresponding on average to approximately one polar amino acid every three heptad repeats (Table S1). Notably, the propensity to accommodate polar amino acids decreases as the number of helices forming the coiled-coil assembly increases. The frequency of polar amino acids is highest at 18.8% in coiled coils formed by two helices, and it decreases to 14.1% and 11.7% for three-stranded and four-stranded coiled coils, respectively. In contrast, 30% of the "*a*" and "*d*" positions in *E. coli* FtsLB are polar, confirming that the level of enrichment is quite high in comparison with the average coiled coil and nearly three times the average frequency for coiled coils that assume a tetrameric configuration, suggesting that the coiled coil of FtsLB is not designed for maximum stability.

The polar cluster is evolutionarily conserved

To investigate if the polar cluster is a conserved feature of FtsLB, we analyzed a multisequence alignment containing 2900 pairs of FtsB–FtsL sequences from diverse proteobacterial taxa. In *E. coli*, the coiled-coil region is predicted to extend for approximately five heptad repeats, starting after the transmembrane helices and ending approximately at the CCD region (29). Three polar amino acids are found in FtsB at positions *2d* (Gln-39, the "*d*" position in the second heptad repeat), *3a* (Asn-43), and *4a* (Asn-50). FtsL contains two arginine residues at positions *2a* and *3a* (Arg-67 and Arg-74, respectively). In addition, FtsL contributes Glu-88 (*5a*), one of the critical amino acids in the CCD region (21, 24), at the margin of the coiled coil.

The pattern of polar/nonpolar amino acids found at "*a*" and "*d*" positions in the alignment is summarized graphically in Figure 3. We found that this feature is highly conserved, even if the specific sequence is not. As highlighted by the main "*paths*" in the graph, five of the six polar positions in *E. coli* have a strong tendency to be polar in all species. The only position at which a polar amino acid is not particularly conserved corresponds to Arg-67 (*2a*) of FtsL. However, a polar amino acid occurs overall frequently across any of the "*a*" and "*d*" positions of the first two heptad repeats (71% of the sequences). In fact, the class of sequences to which *E. coli* belongs (*i.e.*, those sequences in which both FtsL and FtsB contribute three polar amino acids each) is the most common (39%). Moreover, 84% of the sequences contain at least five

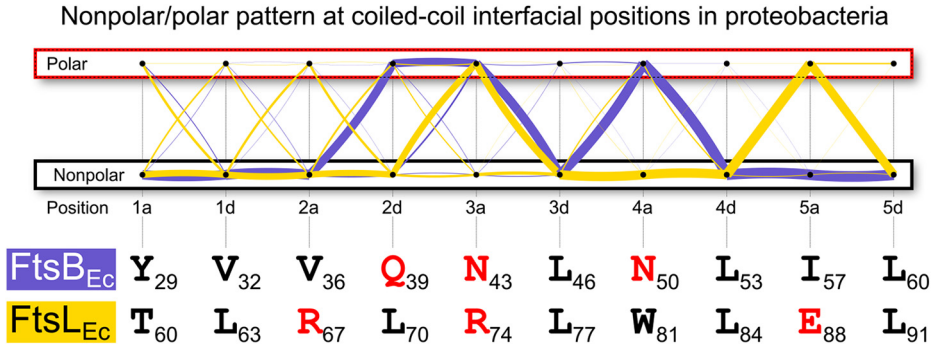

Figure 3. Conservation of the polar cluster in the core "*a*" and "*d*" positions of the coiled coil of FtsLB in proteobacterial species. The *yellow* (FtsL) and *blue* (FtsB) *lines* follow the pattern of polar (Asp, Glu, His, Arg, Lys, Gln, and Asn) and nonpolar amino acids in alignments of 2900 paired FtsB/FtsL sequences. The thickness of the *lines* is proportional to the number of sequences that follows a certain (polar/nonpolar) binary pattern. The graph evidences that polarity at positions corresponding to Gln-39, Asn-43, and Asn-50 is a highly conserved feature in FtsB. Positions Arg-74 and Glu-88 are also most frequently polar in FtsL. Polarity at the position corresponding to Arg-67 is not conserved in FtsL. However, there is overall a 71% probability that at least one position in the first two heptad repeats of FtsL contains another polar residue.

polar amino acids (Fig. S1). The analysis therefore suggests that, in proteobacteria, the coiled coil of FtsLB is far from being tuned for maximum stability and is thus designed to be dynamic or metastable for functional reasons.

The polar cluster tunes the propensity of FtsLB to transition to an activated state

In order to test whether the conserved polar cluster is critical for function, we expressed mutant variants at these positions *in vivo* and examined whether these changes led to cell division defects. In our first round of experiments, we tested the effect of "idealizing" the coiled coil by converting each of the polar amino acids to a canonical hydrophobic residue (Ile or Leu, at "*a*" and "*d*" positions, respectively). We also mutated Trp-81 of FtsL to a smaller hydrophobic residue, since bulky aromatic residues tend to be excluded from natural coiled-coil interfaces (40). The effect of individual point mutations was assessed in complementation experiments in which we measured the length distribution of samples of at least 500 cells. As done previously to assess the severity of mutations that cause elongation defects (29), we measured the proportion of cells with lengths exceeding the 95th percentile of the length distribution observed for the WT (*dashed vertical line* in the four example length distributions displayed in Fig. 4, *A–D*). The fraction of elongated cells is reported for further mutants in the histograms in Figure 4, *E–H*, grouped for FtsB nonideal-to-ideal, FtsL nonideal-to-ideal, FtsL charged-to-charged, and double substitutions at positions R67 and R74 in FtsL. Pictures, cell distributions, and metrics for all mutations are reported in Figure S2.

Three of the five polar-to-nonpolar individual point mutations tested (FtsB Q39L and N50I; FtsL R67I) resulted in notable defective phenotypes, displaying a fraction between 12 and 37% of elongated cells (Fig. 4, *E* and *F*). The remaining two polar-to-nonpolar mutations (FtsL R74I and FtsB N43I) were similar to WT. Mutation of the bulky Trp residue in FtsL (W81I) also resulted in a defective phenotype. To exclude that the division defects were due to changes in protein expression levels, we performed Western blot analyses (Fig. S3), which indicated that each mutant was expressed to similar levels as WT, except for FtsB N43I, which showed increased expression. These observations support the hypothesis that the polar cluster plays a critical role in FtsLB function.

Arginine is one of the most polar amino acids, essentially never occurring in its neutral form, and thus it is one of the most destabilizing amino acids when buried within a protein core. For this reason, we further investigated the effects of mutating both Arg-67 and Arg-74 in FtsL (Fig. 4*H*). The double charged-to-hydrophobic mutation (R67I + R74I) resulted in impaired division in a manner similar to the R67I single mutant (30% *versus* 33% elongated cells). We then asked whether the identity of these positions is important (Fig. 4*G*). We first inverted the charge with Glu substitutions. The R67E mutation produced a division-defective phenotype (33% elongated cells) similar to that of R67I. Like the Ile substitution at the same position, R74E did not result in elongation, but somewhat surprisingly, this substitution resulted in a larger fraction of smaller cells (left-shifted peak compared with WT; Fig. 4*D*). We then preserved the positive charges at the 67 and 74 positions of FtsL with Lys substitutions. R67K produced WT-like cells, whereas R74K had a similar phenotype to R74E, with a larger fraction of small cells (Fig. S2*C*).

The fact that charge reversal mutations at positions R67 and R74 result in opposite phenotypes (elongation *versus* small cells, respectively) is interesting. Gain-of-function mutations in FtsLB that cause early cell division have been identified before (21, 24), predominantly within the CCD. The reduced cell length of R74 mutants is particularly notable since a similar phenotype was never observed among a total of 55 mutations in the transmembrane region and coiled-coil positions of FtsLB that were assessed in our previous analysis with identical conditions and methodology (29). For this reason, we combined both charge reversal mutations (R67E + R74E) to observe their interplay. Interestingly, R67E + R74E resulted in a shorter cell length distribution (13% elongated cells

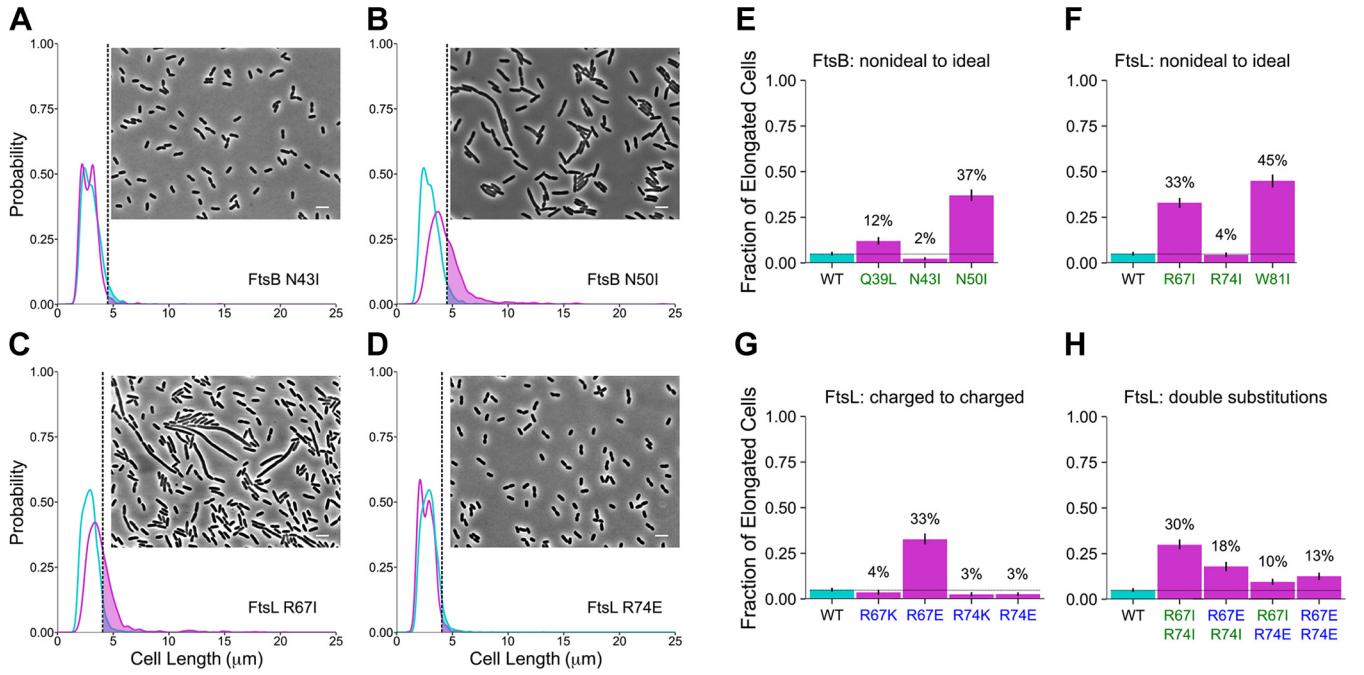

Figure 4. Mutations in the polar cluster cause both elongation and small cell phenotypes *in vivo*. *A–D,* phase-contrast images of representative mutants (scale bar represents 5 μm) and cell length distributions of mutant cells (*magenta*) compared with WT (*cyan*). The *shaded areas* to the *right of the dotted lines* represent the elongated cells (*i.e.*, those that are longer than the 95th percentile in the WT distribution). The four examples include (*A*) a WT-like mutant (FtsB N43I), (*B* and *C*) two mutations that cause frequent elongation (FtsB N50I at 37% elongated and FtsL R67I at 33% elongated), and (*D*) a mutant that displays a higher fraction of shorter cells (FtsL R74E). Pictures, cell distributions, and metrics for all mutations are reported in Figure S2. *E–H,* histograms of percent of elongated cells for all mutations at the nonideal coiled-coil positions (nonpolar mutations in *green*; charged mutations in *blue*). These include (*E*) FtsB and (*F*) FtsL nonideal-to-ideal mutations, (*G*) FtsL charged-to-charged mutations, and (*H*) FtsL double mutations at positions R67 and R74. Nonideal-to-ideal mutations tend to cause notable elongation phenotypes. A remarkable exception is position R74, in which mutations appear to cause a small cell phenotype (likely because of deregulated division). R74E, in particular, suppresses the elongated phenotypes of R67I and R67E, indicating that these positions are important for governing the fine balance between the *on* and *off* conformations of FtsLB. Experiments were performed at 37 °C. Error bars represent the 95% confidence interval of the fraction of elongated cells estimated from 1000 replicates of bootstrap resampling.

compared with 33% for R67E alone; Fig. 4*D*), supporting the hypothesis that R74E can suppress the R67E elongation defect by inducing early cell division. This is also consistent with the phenotypes we observed in the R67I + R74E (Fig. 4*H*) and R74E + W81I (Fig. S2*D*) double mutations (10% and 15% elongated cells, respectively), where the elongated phenotypes of R67I and W81I alone (33% and 45% elongated cells, respectively) are also suppressed, resulting in a decreased fraction of elongated cells.

In order to determine if FtsL R74E is unique or if other mutations at that position can suppress elongation defects, we tested further combinations. Ultimately, we found that the extent of observed suppression varies with the identity of the amino acid at position 74. The charged-to-nonpolar mutation R74I (which was WT-like alone and did not suppress the elongated phenotype of R67I) also appears to reduce the severity of the elongated phenotype when combined with R67E (33% *versus* 18% elongated cells for R67E and R67E + R74I, respectively). On the other hand, R74K did not noticeably suppress the elongation defect when combined with R67I, R67E, or W81I (Fig. S2*D*), suggesting that a negative charge at position 74 (or perhaps merely the lack of a positive charge) is needed for the suppression effect.

Overall, the data suggest that the polar cluster of the FtsLB coiled coil is important for fine-tuning the propensity of the complex to transition to an activated state. In particular, the Arg residues at the 67 and 74 "*a*" positions in FtsL somehow play opposing roles in this regulation, and their specific residue identity is important.

Hydrophobic substitutions in vitro *increase thermal stability*

If the polar cluster plays a role in tuning the propensity of FtsLB to transition to an activated state, then polar-to-nonpolar substitutions likely stabilize the coiled-coil domain but may be detrimental for the complex to undergo conformational changes. To directly assess whether the polar cluster does in fact govern the structural stability of FtsLB, we investigated the thermal stability of the complex *in vitro* by monitoring secondary structure content using CD. In this experiment, we simultaneously mutated all four centrally located polar residues in both FtsB (Q39L and N43I) and FtsL (R67I and R74I).

We used a version of FtsL ($FtsL_{35–121}$) lacking the unstructured N-terminal tail, which is not necessary for the assembly of the FtsLB complex (29). Both FtsB and FtsL constructs retained the N-terminal purification tags (His and Strep tags, respectively), which do not cleave efficiently. To avoid interference from reducing agents in the sensitive UV region, both native cysteine residues of FtsL were replaced

with alanine (C41A and C45A). We have shown previously that this Cys-less construct is stable and functional (29). The resulting constructs, His-FtsB/Strep-FtsL$_{35-121}$–C41A–C45A and His-FtsB–Q39L–N43I/Strep-FtsL$_{35-121}$–C41A–C45A–R67I–R74I, are termed "WT" and "4×-mutant," respectively.

Figure 5*A* shows the CD spectra of the constructs solubilized in *n*-dodecyl-β-D-maltopyranoside (DDM) at low temperature (4 °C). Both constructs have the expected spectral signature of helical proteins with high secondary structure content. Little difference is noticeable between the two constructs, suggesting that the four mutations do not cause major changes in helical content at low temperature. We then investigated the difference in stability between WT and 4×-mutant comparing the CD signal at increased temperatures, monitoring ellipticity at one of the helical minima (224 nm; Figs. 5*B* and S4).

The WT construct (*blue dots*) displays a sigmoidal melting curve with a transition centered around 40 °C. Given the high thermal stability of transmembrane helices, the transition is most likely attributable to loss of helicity in the coiled-coil region. The relatively early unfolding transition confirms that the coiled coil of FtsLB is structured but not optimized for stability. The melting curve of the 4×-mutant is markedly different (*red dots*). The construct retains a higher degree of secondary structure at higher temperatures, indicating that, as expected, the replacement of unfavorable polar side chains for canonical hydrophobic residues stabilized the coiled coil. However, the 4×-mutant's curve does not display the same degree of cooperativity as the WT, but rather, it shows a nearly linear loss of ellipticity lacking a clear transition. A sharp transition is consistent with a two-state unfolding process typical of well-folded proteins; therefore, it is likely that the 4×-mutant version of the coiled coil of FtsLB can access alternative and potentially misfolded conformations. This notion becomes particularly interesting in light of the fact that FtsLB can be modeled in two alternative conformations, as discussed in the next section.

An alternative structural organization for FtsLB: the Y-model

Experimental evidence *in vitro* indicates that the FtsLB complex is a 2:2 FtsL:FtsB tetramer (28, 29, 36). We previously modeled the complex in the simplest configuration consistent with this tetrameric state (*i.e.*, a monolithic four-helix bundle that extended across the transmembrane and periplasmic regions (29); Fig. 2*A*). We noted, however, that it is unlikely that a tetrameric coiled coil would be stable with the number of polar residues present in its core. Consistently, the coiled-coil configuration did not appear stable during molecular dynamics (MD) simulations, where we observed a marked tendency of this region to open and recruit water within its interior.

The previously discussed analysis of the structural databases indicates that a polar coiled coil would be most likely to assume a two-stranded configuration. Experimental studies on model coiled coils also indicate that polar residues in core positions can influence the number of helical strands in coiled coils, with a two-stranded coiled coil being better suited to accommodate polar residues (41, 42). In particular, the four Arg residues contributed by the FtsL chains (two from each monomer) are particularly costly to bury, since Arg is essentially always protonated even in a hydrophobic environment. Indeed, a systematic study of all 20 amino acids in a coiled-coil model found that Arg is the most destabilizing residue at "*a*" positions and also that, when present, this amino acid strongly favors a two-stranded over a three-stranded configuration (43). This finding is in good agreement with our analysis of the structural database, which shows that Arg is relatively frequent at "*a*" positions in two-stranded coiled coils (4.5%) but much

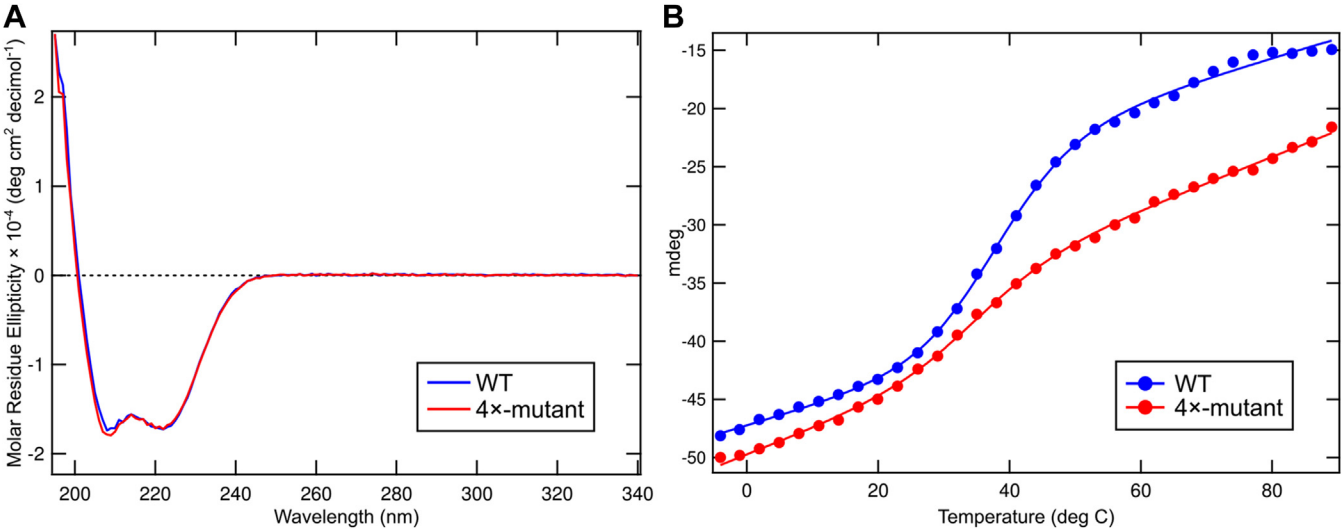

Figure 5. Conversion of the polar cluster to idealized hydrophobic residues increases thermal stability but affects folding cooperativity. *A,* Far-UV CD spectra of WT FtsLB (*blue*) compared with the 4×-mutant (*red*) at 4 °C. *B,* representative temperature melting curves comparing WT FtsLB (*blue*) to the 4×-mutant (*red*). The WT melting curve displays a sigmoidal transition centered around 40 °C. In contrast, the 4×-mutant displays a curve that is shifted to the *right* but lacks a significant transition, possibly indicating a loss of cooperativity of unfolding. CD scans were monitored at 224 nm from 4 to 89 °C. Replica melting curves are included in Fig. S4.

more rare in four-stranded coils (0.5%; Table S1). This preference can be explained by the solvent accessibility of the side chains: in two-stranded coiled coils, the narrower interface allows the polar moieties at the end of the side chains to access the surrounding solvent and remain partially water exposed. As the size of the helical bundle increases, these groups become increasingly more buried, resulting in a higher desolvation cost.

Following the lead suggested by the MD analysis of our original FtsLB model (29), we report a revised model of FtsLB in which the periplasmic region splits into a pair of two-stranded coiled-coil domains, each containing one FtsL and one FtsB chain (Fig. 6*A*). This model (which we named the "Y-model" from its shape) is based on the same set of side-chain contacts between FtsB and FtsL inferred by the coevolutionary analysis we used to derive the original monolithic model (29) (named here the "I-model"). The transmembrane region is modeled in the same four-helix bundle configuration of the original I-model. As in the I-model, the helix of FtsL in the coiled-coil region is continuous with the transmembrane helix, as indicated by experimental analysis (29). In this configuration, the FtsL helix remains on the outward face of the "Y," whereas the helices of FtsB occupy the inward face, in close proximity to each other and thus buried within the overall arrangement. With respect to the transmembrane domain, the helix of FtsB is rotated so that its interfacial "*a*" and "*d*" positions face the corresponding positions of FtsL, a rotation that is readily enabled by the structurally malleable Gly-rich linker that occurs between the transmembrane and coiled-coil helices of FtsB (29, 36).

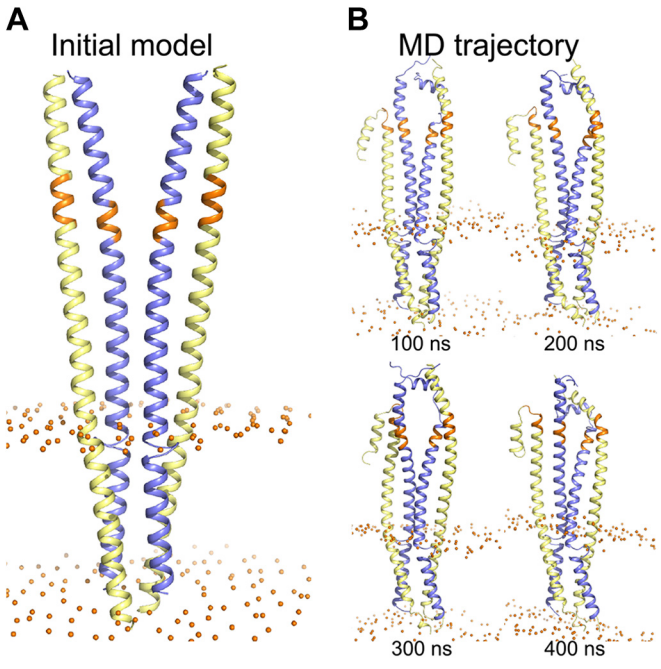

Figure 6. The Y-model of the FtsLB complex. *A,* initial model. The model has the same transmembrane region of the original I-model. The coiled-coil region was modeled as a pair of two-stranded coiled-coil domains, each containing one FtsL and one FtsB helix. The modeling is based on the same set of side-chain contacts between FtsB and FtsL inferred by the coevolutionary analysis used to derive the I-model. Colored in *orange* is the CCD region. *Spheres*: lipid headgroup phosphate P atoms. *B,* four frames of the trajectory of a 400 ns molecular dynamic run of the Y-model. The transmembrane and coiled-coil regions remain relatively stable during the entire trajectory. The helices tend to break and occasionally unfold in correspondence of a predicted hinge near the CCD region (*orange*). The RMSD analysis of all three replica runs is reported in Fig. S6 and Table S3. CCD, constriction control domain.

AlphaFold2 modeling of FtsLB supports the structural features of the Y-model

With the outstanding performance of the program AlphaFold2 (45) at the recent CASP14 structural prediction competition, we decided to compare prediction of the FtsLB complex obtained with this method to our models. AlphaFold2 produced five models for FtsLB, which are ranked by their confidence score (Fig. S5 and Table S2). Although the program was given a 2:2 FtsL:FtsB stoichiometry as the input, only the fifth ranked model produced a tetramer. Interestingly, the fifth model assumed a configuration that roughly resembles the Y-model, with its tetrameric assembly being mediated by the transmembrane region and two separated two-stranded coiled-coil domains (Fig. S5*A*). However, rank model 5 and the Y-model align poorly (Cα RMSD of 11.11 Å). It should be noted that rank model 5 is a low-confidence model that is very loosely packed in its transmembrane region, and thus, it is unlikely to be a good candidate for the structure of FtsLB.

The top four ranked AlphaFold2 models form two separated FtsB–FtsL heterodimers (Fig. S5*A*). This is contrary to our experimental evidence, which indicates that FtsLB forms a heterotetramer (28, 29). In spite of this difference, however, ranked models 1 to 4 are structurally very similar to each half of the tetrameric Y-model (Cα RMSD values of 2.26–2.35 Å; Table S2), whereas their alignment with the I-model is less optimal (Cα RMSD values of 3.26–3.47 Å). The AlphaFold2 models also display the same distinctive structural features that we identified, with identical interfaces, an unwound loop in the Gly-rich linker, and FtsL in a continuous helical configuration through the transmembrane and coiled-coil domains. The superimposition of AlphaFold2 ranked model 1 against the Y-model in Figure S5*C* clearly illustrates that the two models are in excellent agreement. In summary, aside from the stoichiometry of the complex, the AlphaFold2 results provide a useful and independent validation of the structural organization of the Y-model.

The Y-model remains more stable in comparison to the I-model during MD simulations

To assess the stability of the Y-model and its dynamic properties, we performed MD simulations in explicit 1-Palmitoyl-2-oleoyl-*sn*-glycero-3-phosphoethanolamine bilayers in conditions analogous to the previous MD simulations of the I-model (29). As done previously, the coiled coil was extended in the initial configuration by approximately 20 amino acids beyond its likely boundaries (the CCD region) to avoid end effects. We will refer to this C-terminal region (residues 92–110 for FtsL and residues 62–79 for FtsB) as the post-CCD region. Three replica MD simulations were run for 400 ns each. The three trajectories are illustrated in Figure 6*B*

and, in more detail, in Figure S6. Overall, we observed that the Y-model remained stable during the simulation time.

Similar to our previous simulations (29), the transmembrane region underwent only minor rearrangements, with average RMSDs of 2.4, 1.6, and 1.8 Å in the three replica runs (Fig. S6, *red traces*, and Table S3). We found that the reconfigured coiled-coil region of the Y-model was very stable across all three replica runs with 1.4 to 1.7 Å average RMSDs (*green and blue traces*). For comparison, the average RMSDs for the same region of the I-model were 2.3 to 3.4 Å (29). The fact that the coiled coil of the Y-model remained well structured is in stark contrast with the simulation of the I-model, during which the four-stranded coiled coil opened, allowing water molecules into the core and in contact with the polar cluster.

As hypothesized, the terminal polar moieties of the long side chains (the amide group of FtsB Gln-39 and the guanidinium group of FtsL Arg-67 and Arg-74) are partially solvent exposed in the two-stranded coiled coils of the Y-model, whereas their nonpolar CH_2 groups contribute to hydrophobic packing at the interface. Solvent accessible surface area calculations indicate that on average the amide group of FtsB Gln-39 remains 20 to 40% solvent accessible, and the guanidinium groups of FtsL Arg-67 and 74 remain 40 to 60% accessible. The only polar group that remained nearly completely buried in the coiled coil was the shorter Asn-43 of FtsB, but its hydrogen bonding potential is satisfied by interacting with the backbone carbonyl group of Leu-70 and often with the side chain of Glu-73 on the opposed FtsL chain. In fact, the four side chains of the polar cluster tend to interact with each other in a shared network of hydrogen bonds (Fig. 7*B*). Overall, the organization of the polar cluster appears clearly more favorable in the Y-model in comparison with the I-model, in which these positions were unfavorably buried in a four-helix coiled-coil conformation.

The coiled coils displayed a tendency to break near the CCD region, in correspondence to a likely hinge that contains Gly residues in both FtsB (positions 62 and 63) and FtsL (position 92). The terminal segments beyond this section are highly dynamic in our simulations, as indicated by their high RMSD traces (Fig. S6, *orange and purple traces*). This is primarily because of the lever arm effect, since most of the RMSD arises from propagation of the unfolding of the hinge region, whereas the helical portion past the hinge stays mostly helical. The post-CCD segment of FtsB is essential for binding to FtsQ (46, 47) and is known to be structured in the FtsQLB complex (34, 35). This segment forms an 11-residue helix that starts right after the predicted hinge (position 64) and then associates with the C-terminal β-sheet of FtsQ by β-strand addition. FtsQ was not included in our simulations, and thus, it is not surprising that the C-terminal peptides unfolded in the simulation, although significant helical content was generally retained. The structure of the C-terminal segment of FtsL is not known, although presumably this terminal tail is also structured in the presence of FtsQ (or other components). In our simulations, this segment also tends to extend at the predicted hinge but otherwise retains significant helical content, similar to the corresponding segment of FtsB.

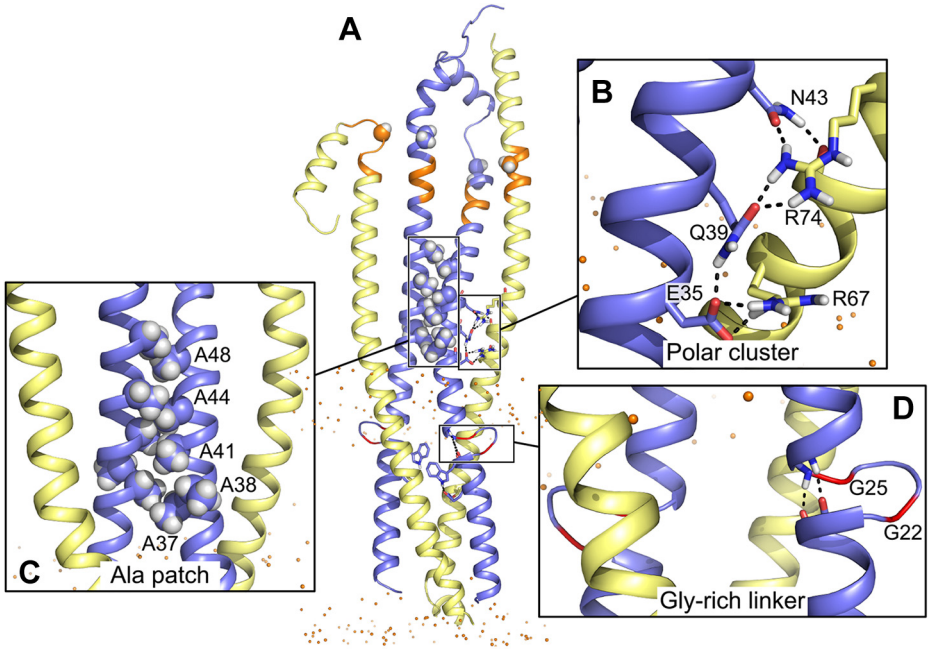

Figure 7. Features of the Y-model. *A,* MD frame of the Y-model highlighting three features of interest. *B,* the amide group of FtsB Gln-39 and the guanidinium group of FtsL Arg-67 and Arg-74 are partially solvent exposed, whereas only the shorter FtsB Asn-43 is mainly buried. The polar cluster side chains tend to interact with each other in a shared network of hydrogen bonds. *C,* a patch of Ala residues on the opposite face of the FtsL/FtsB coiled-coil interfaces mediates the interaction of the two FtsB helices. The interaction is stable through the entire replica MD runs. *D,* the FtsB Gly-rich linker forms a short loop of four amino acids. The helical termini of the transmembrane and coiled-coil helices remain in contact in a configuration that resembles a continuous helix. There is hydrogen bond formation between the carbonyl groups of transmembrane residues 19 to 20 and the N–H groups of residues 26 to 27 of the coiled coil. MD, molecular dynamics.

An Ala-rich patch in FtsB mediates intercoil contact in the Y-model

An interesting outcome of the MD simulations is a small but significant rearrangement of the two branches of the "Y." The two coiled-coil domains are separated by approximately 7 Å in the initial model, but this gap closes in the simulations. After this closure, the domains remain in permanent contact during all runs. Their contact is mediated by a mildly hydrophobic patch in FtsB consisting of five Ala residues that are clustered on the solvent-exposed back side of the helix (positions 37, 38, 41, 44, and 48; Fig. 7*C*). This interaction results in an additional helix–helix interface with an ∼1000 Å^2 contact area spanning approximately three helical turns and a right-handed crossing angle of approximately −35°.

The interaction forms rapidly within a few nanoseconds in runs 1 and 2. Once the contact is established, it persists for the entirety of the 400 ns runs, and thus, the two branches of the "Y" become locked into proximity. Only in replica run 3, the branches initially splay apart forming a more open "Y," and it takes almost 40 ns for the branches to come in contact. In this run, when the contact is formed, it is not symmetrical, involving Ala residues 41, 44, and 48 on one chain packing with residues 37, 41, and 44 in the other chain. Once this interaction is established, it also persists for the entirety of the 400 ns simulation, but it does not revert to the nearly symmetrical conformation observed in the other runs. Because of the asymmetry, one coil of FtsB appears to be pulled away from the transmembrane region, thus stretching the Gly-rich loop and breaking the contact between the termini of the transmembrane and coiled-coil helices.

To test whether the Ala patch is an essential feature of FtsLB, we drastically mutated the Ala residues and measured the resulting cell length phenotypes *in vivo*. All five Ala residues were mutated at once to combinations of Asp and Glu (AAAAA → EEEDD and AAAAA → DDDEE), according to the hypothesis that the replacement of hydrophobic Ala with negatively charged amino acids should destabilize the interaction interface. As shown in Figure 8, the mutations did not cause elongation phenotypes, but their distributions were enriched in smaller cells compared with WT (median length of 2.74 and 2.69 μm for the EEEDD and DDDEE mutants, respectively, compared with 2.93 μm for the WT), in a fashion that is similar to the FtsL R74E mutant discussed previously.

Perhaps surprisingly, our experiments indicate that the disruption of the Ala patch feature does not cause major loss of function. If the Y-model is an accurate representation of the FtsLB complex, the data indicate that the added stability deriving from the interaction of the two coiled-coil branches is not a strong requirement. However, the observed enrichment in small cells is consistent with the hypothesis that fine-tuning the stability of the coiled coil participates in governing the balance between the *on* and *off* states of the complex. Specifically, it suggests that destabilization of the coiled coil tends to favor unregulated (early) cell division. It remains to be confirmed whether the hypothesized destabilization arises from the loss of the interbranch hydrophobic interface or from direct destabilization of the coiled coil because of the presence of a patch of negative residues.

The AWI positions of FtsL are surface accessible in an initial model of the FtsQLB complex

The CCD and AWI positions are located in a region near the end of the predicted coiled coil in FtsLB, preceding a likely hinge created by three Gly residues in close proximity (positions 62–63 in FtsB and position 92 in FtsL). CCD mutants rescue a *ΔftsN* phenotype, suggesting that they induce changes in the FtsLB complex that mimic the activation signal given by FtsN (21, 24). This process likely involves a conformational change that makes the AWI positions of FtsL available for interacting with FtsI, leading to activation of septal PG synthesis (25, 26).

In the Y-model, the AWI positions (82–84, 86–87, and 90) of FtsL are completely solvent exposed. Given that FtsLB exists as a complex with FtsQ, we assembled a preliminary model of the FtsQLB complex by aligning the region of FtsB that is in common between the Y-model and the cocrystal structure of

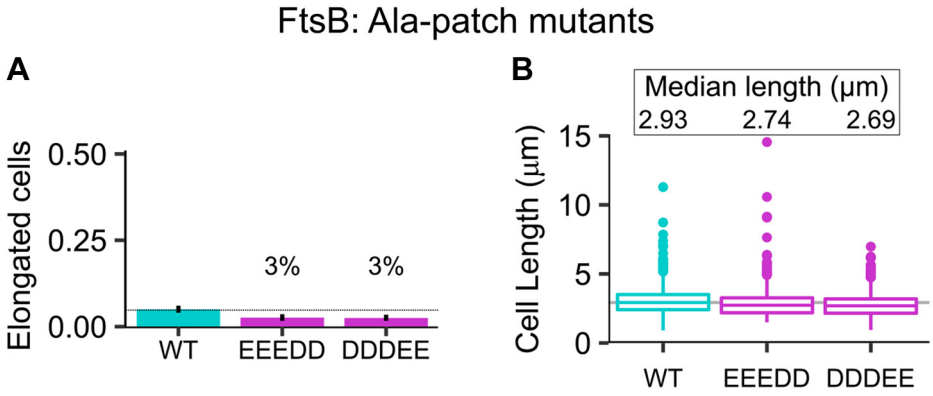

Figure 8. Disruption of the Ala patch of FtsB results in smaller cells. A mildly hydrophobic patch of Ala residues is predicted to mediate the interaction of the two FtsB helices in the Y-model. All five Ala positions (37, 38, 41, 44, and 48) were simultaneously replaced with negatively charged residues, with a combination of three Glu and two Asp residues (EEEDD) and vice versa (DDDEE). *A,* fraction of elongated cells for the mutants. Error bars represent the 95% confidence interval, estimated from 1000 replicates of bootstrap resampling. *B,* median cell length distributions. The disruption of the potential interaction interface does not yield a defective division phenotype; however, a shift of the distribution with an increase of small cells suggests that the disruption of the Ala patch induces some level of disregulated triggering of early cell division. Experiments were performed at 37 °C. Cell distributions are plotted in Fig. S2*E*.

the C-terminal FtsB fragment in complex with FtsQ (Protein Data Bank [PDB] code: 6H9O (35)). This fragment starts with the post-CCD helix (residues 64–74), following the putative hinge at the end of the coiled coil (residues 62–63). Because of the flexible hinge, the orientation of the post-CCD helix is uncertain. However, the N terminus of the periplasmic domain of FtsQ needs to be near the lipid bilayer for proper placement of its transmembrane helix. We found that by modeling the post-CCD helix as a nearly straight continuation of the coiled-coil helix, this constraint is satisfied and FtsQ is oriented in a position that does not collide with the FtsLB complex.

In this preliminary structural model of the FtsQLB complex (illustrated in Fig. 9, *A* and *B*, with FtsQ depicted in *gray*), the surface of the coiled-coil region of FtsB is almost completely occluded. The helices of FtsB are flanked on one side by FtsL and on the opposite side by the helix of FtsB from the opposite coiled coil, and their remaining exposed face is then occluded by FtsQ. Conversely, the helix of FtsL packs only with its partner FtsB helix, whereas the opposite helical face remains exposed to solvent even in the presence of FtsQ. Interestingly, all amino acids of the AWI region of FtsL (in *green*) occur in this face and thus remain solvent exposed. This configuration supports the AWI region as a good candidate surface for interaction with FtsWI. Conversely, the coiled coil of FtsB, which is nearly completely buried in the Y-model, would require major structural rearrangements to become available.

Conclusions

In this article, we address the hypothesis that the coiled coil of FtsLB is a critical functional element. We explore the role of an unusual cluster of polar amino acids that occur at core positions within this domain and investigate whether the stability of the coiled coil is marginal by design. We propose that this characteristic may be critical for enabling the hypothesized FtsLB *off/on* transition that leads to the activation of the PG synthase machinery. Our evidence indicates that mutations affecting the conserved polar cluster lead to appreciable division phenotypes, indicating that this feature is functionally important. The fact that mutations to hydrophobic residues increase thermal stability *in vitro* but often lead to division defects *in vivo* suggests that the coiled-coil domain is indeed likely to be a "detuned" functional element, sacrificing some of the stability of the complex in order to enable proper function.

In addition to affecting the plasticity of the coiled coil, the polar cluster likely contributes to the shape of the periplasmic domain by causing it to branch out, as proposed in the revised Y-model of the complex. The branched Y-model satisfies all the known constraints (*i.e.*, oligomeric state, inferred amino acid contacts, and mutagenesis data) as well as the original I-model, but it appears to be structurally more stable when assessed by MD, unlike the I-model in which the coiled coil was rapidly infiltrated by water during its simulation (29). The structural arrangement of the Y-model is also in better agreement with predictions from AlphaFold2, after accounting for discrepancies between their overall stoichiometries. For these reasons, we propose the Y-model as the more likely configuration of the FtsLB complex.

This hypothesis that the polar cluster shapes the coiled coil into independent branches offers an interpretation for our observation *in vitro* that the "idealized" coiled coil (the "4×-

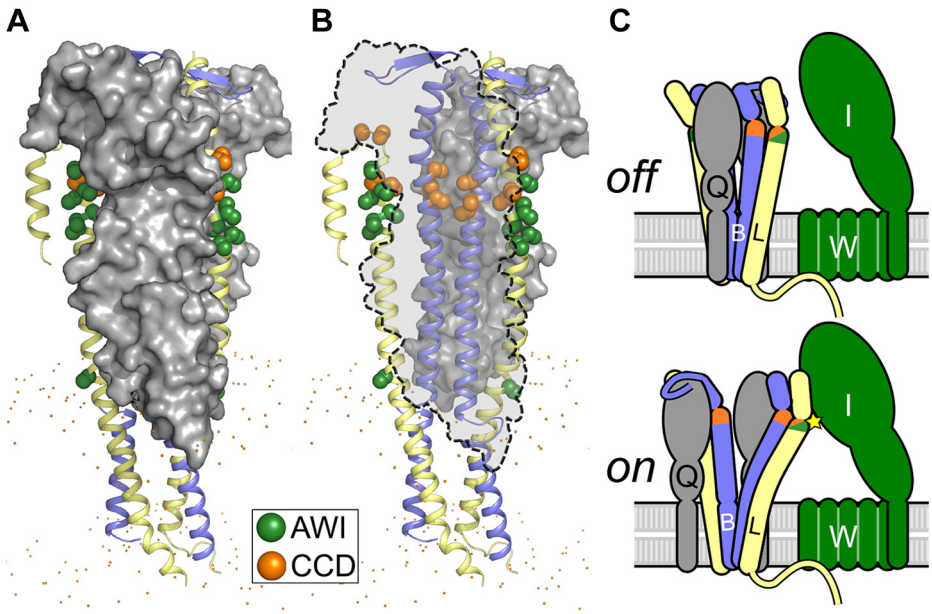

Figure 9. A structural shift in the coiled coil of FtsLB may be involved in its activation. *A,* preliminary model of the FtsQLB complex, obtained by aligning the region of FtsB that is in common between the Y-model and the crystal structure of FtsQ (Protein Data Bank code: 6H9O). In this model, the four helices of the coiled coil of FtsLB form a flat bundle sandwiched between the two periplasmic domains of FtsQ (*gray*). *B,* see-through representation of the same model, with one of the two FtsQ subunits removed and represented by a *dashed outline*. The positions of the CCD and AWI domains of FtsB and FtsL are highlighted as *orange* and *green spheres*, respectively. FtsB is nearly completely buried. FtsL is more solvent exposed, and its AWI positions occur on a solvent-facing surface. *C,* schematic representation of a potential model for FtsLB activation. A structural shift involving the coiled coil of FtsLB (potentially involving the separation of the two branches) exposes the AWI region of FtsL to a hypothesized protein–protein interaction with FtsI (*star*). This transition may be favored by destabilization of the coiled-coil region. AWI, activation of FtsWI; CCD, constriction control domain.

mutant" $FtsB_{Q39L,N43I}/FtsL_{R67I,R74I}$) unfolds at higher temperatures but displays a broad noncooperative transition—an indication that the complex may assume multiple alternative configurations. In the "idealized" mutant, the coiled coil would not pay a steep penalty (*i.e.*, the burial of polar side chains) to continue in the same four-stranded configuration of the transmembrane region, thus it is possible that a competition could occur between the I and Y configurations.

One of the most interesting outcomes of this analysis is the discovery of suppressor mutations that occur within the polar cluster. Specifically, changes in FtsL at position Arg-74 can suppress the phenotype of mutations at position Arg-67. The observations suggest a likely structural interplay between the two positions, where mutations cancel each other's opposing tendencies to make division less likely (R67I and R67E, which display moderate elongation) or more likely (R74E, which is enriched in smaller cells), suggesting that these positions fine-tune the interactions that govern the balance between the *on* and *off* states of the complex. In addition, we noted that disruption of the mildly hydrophobic Ala patch (EEEDD and DDDEE mutants) that mediates the contact between the two branches of the coiled coil in the Y-model MD simulations also results in a smaller than normal cell distribution. This finding suggests that separation of the branches, which would be favored in the EEEDD and DDDEE mutants, facilitates the *on* transition. It is unclear if the R74E mutation operates in a similar manner, although in the model, substitution of R74 disrupts an intricate network of hydrogen bonding that connects the entire polar cluster, as illustrated in Figure 7*B*.

We propose a model in which the stability of the FtsLB coiled coil needs to be perfectly tuned. If the coiled coil is too stable, the complex does not respond appropriately to the FtsN-derived stimulus that normally causes activation of the complex. Conversely, if the coiled coil is further destabilized, FtsLB can become activated in an unregulated manner. Functional and metastable coiled-coil domains are known to be critical for other bacterial signaling processes such as those involving two-component systems (48), in which the coiled coil functionally connects the membrane-bound sensory domain with the response kinase domain in the cytoplasm. Specific examples include the *Staphylococcus aureus* antibiotic sensor NsaS (49), the *Bacillus subtilis* thermosensor DesK (50, 51), and the *Bordetella pertussis* virulence factor BvgS (52), each of which contains a coiled-coil domain with nonideal residues that enable conformational changes needed to regulate signaling activity. For these systems, the degree of hydrophobicity of the coiled-coil interface impacts the rigidity of the sensor and can even directly modulate the balance between kinase and phosphatase activity (51, 52). The presence of nonideal residues at the interface of the FtsLB coiled coil suggests that a similar "tuning" of stability may be needed to support conformational rearrangements.

Further structural and biophysical characterization is necessary to validate this model of FtsLB and to fully understand how the structural organization of the coiled coil and its conformational changes operate in triggering septal PG reconstruction.

Experimental procedures

Plasmid cloning

For the *in vivo* complementation experiments, mutant variants of FtsB or FtsL were cloned *via* standard QuikChange mutagenesis or inverse PCR into pMDG7 (47) (flag3-FtsB) or pMDG29 (30) (flag3-FtsL), respectively. For the CD experiments, the His-tagged FtsB and Strep-tagged Cys-less (C41A and C45A) $FtsL_{35–121}$ were ligated into a modified pETDuet-1 vector at restriction sites NcoI/HindIII and NdeI/XhoI, respectively. Point mutations were introduced using standard QuikChange mutagenesis. All constructs were confirmed by DNA sequencing (Quintara Biosciences). A complete plasmid inventory is included in Table S4.

Bacterial strains, plasmids, and media for in vivo experiments

The phenotypic analyses were performed using depletion strains NB946 (53) for FtsB and MDG277 (47) for FtsL (both obtained from Jon Beckwith *et al.*) in which the WT copy of the protein of interest is under control of a repressible P_{BAD} promoter within the chromosome. These strains were transformed with plasmids containing either WT protein (positive control), empty vector (negative control), or a mutant version of the protein to test for defects in cell division as evidenced by an increase in cell length. For all experiments described, bacterial cells were grown in LB medium supplemented with 100 μg/ml spectinomycin (Dot Scientific) and the appropriate carbon source. Medium was supplemented with 0.2% (w/v) L-arabinose (Sigma) or 0.2% (w/v) D-glucose (Sigma) to induce or repress, respectively, the expression of chromosomal copies of the WT genes regulated by the P_{BAD} promoter. About 20 μM IPTG was added to the medium to induce the expression of mutant genes regulated by the P_{trc} promoter in the plasmid.

Depletion strain experiments

The protocol for the depletion strain experiments was adapted from Gonzalez and Beckwith (47). In short, a mutated copy of FtsB or FtsL was transformed into its respective depletion strain. Strains were grown overnight at 37 °C on an LB plate supplemented with arabinose and spectinomycin. A single colony from the plate was grown overnight at 37 °C in 3 ml of LB medium supplemented with arabinose and spectinomycin. The overnight culture was then diluted 1:100 into fresh LB medium containing the same supplements and grown to an absorbance of ∼0.3 at 600 nm. An aliquot of 1 ml of culture was washed twice with LB medium lacking any sugar and then diluted 1:100 into 3 ml of fresh LB medium supplemented with glucose, IPTG, and spectinomycin to induce expression of the mutated gene in the plasmid and to repress the WT gene in the chromosome. The cells were then grown at 37 °C for 3.5 h, the approximate time necessary to deplete the cells of the WT chromosomal copy (47). The cells were then placed on ice to stop growth before imaging. Depletion strains provided with a WT copy of their respective protein in the plasmid were tested as positive controls, and, similarly,

depletion strains with no protein in the plasmid (empty vector) were tested as negative controls.

Microscopy and cell length measurements

About 10 μl of cell samples were mounted on a number 1.5, 24 × 50 mm (thickness of 0.16–0.19 mm) cover glass slide (Fisher or VWR). Cells were cushioned with a 3% (w/v) agarose gel pad to restrict the movement of the live cells. Cells were optically imaged using a Nikon Eclipse Ti inverted microscope equipped with crossed polarizers and a Photometrics CoolSNAP HQ2 CCD camera using a Nikon 100X oil objective lens. Phase-contrast images of bacterial cells were recorded with an exposure time of 50 ms using Nikon NIS Elements software. Multiple snapshots were collected for each experiment. All images were analyzed to measure the cell length in Oufti (54) using one single optimized parameter set and manual verification. Confidence intervals of the fraction of elongated cells for each mutant were computed from 1000 replicates of bootstrap resampling (55).

Western blots

Expression level across all variants was assessed by Western blot analysis (Fig. S3). About 3 ml of cells were pelleted and resuspended in 300 μl of lysis buffer (50 mM Hepes, pH 8.0, and 50 mM NaCl) with 5 mM β-mercaptoethanol (βME). The cells were sonicated and centrifuged at 21,000*g* for 10 min before collecting the supernatant. Total protein concentration was determined by bicinchoninic acid assay (Pierce). About 120 μl of lysates were mixed with 40 μl of 4× LDS sample buffer (Novex, Life Technologies) with βME and boiled at 98 °C for 3 min. For each FtsL or FtsB sample, the equivalent of 7 μg or 15 μg, respectively, of total protein was separated by SDS-PAGE (Invitrogen) and transferred to polyvinylidene difluoride membrane (VWR). Horseradish peroxidase–tagged anti-FLAG (M2) antibodies (Sigma; 1:1000) were used for immunoblotting analysis.

Protein expression and purification for CD

Plasmids were transformed into BL21(DE3) cells (NEB) and plated overnight at 37 °C on LB agar with 100 μg/ml ampicillin. Cells were washed off the plates with 1 ml LB broth and inoculated into 1 l of ZYP-5052 autoinduction medium as described (56) and grown at 37 °C until reaching an absorbance of ∼0.8 at 600 nm, after which they were incubated overnight at 22 °C. Following expression, cells were pelleted, resuspended in cell wash buffer (100 mM NaCl, 10 mM Hepes, pH 8.0), pelleted again, flash frozen, and stored at −80 °C for future use. The cells were then lysed by sonication in 10 ml/g lysis buffer (50 mM NaCl, 50 mM Hepes, pH 8.0) supplemented with 0.5 mg/ml lysozyme, 5 mM βME, 1 mM phenylmethylsulfonyl fluoride, 1 mM EDTA, and a protease inhibitor cocktail providing (final concentrations) 8 μM leupeptin (Peptides International), 11.2 μM E-64 (Peptides International), 0.32 μM aprotinin (ProSpec), and 0.32 mM 4-(2-aminoethyl)benzenesulfonyl fluoride (Gold BioTechnology). The inclusion body fraction was separated by centrifugation at 10,000*g* for 20 min, followed by ultracentrifugation of the supernatant at 180,000*g* for 30 min to isolate the cell membranes. The FtsLB complex was then extracted from the membrane fraction with lysis buffer supplemented with 18 mM *n*-decyl-β-D-maltopyranoside (Anatrace) and 5 mM βME, rocking at room temperature overnight. Nonresuspended debris was separated from the solubilized protein *via* centrifugation at 10,000*g* for 20 min. The supernatant was added to ∼3 ml of nickel–nitrilotriacetic acid–agarose resin (Qiagen) and rocked for 2 h at 4 °C for batch binding before performing gravity-flow purification. Purification was performed by running 10 column volumes of nickel wash buffer (300 mM NaCl, 25 mM Hepes, pH 8.0, 50 mM imidazole, and 1 mM βME) supplemented with 510 μM DDM (Avanti Polar Lipids), and 10 column volumes of elution buffer (300 mM NaCl, 25 mM Hepes, pH 8.0, 300 mM imidazole, and 1 mM βME) also supplemented with 510 μM DDM. Protein purity was assessed *via* SDS-PAGE (Invitrogen).

CD experiments

Purified FtsLB protein was dialyzed twice at room temperature for at least 2 h into 1 l CD buffer (10 mM phosphate buffer, pH 7.4, and 100 mM NaF) supplemented with 170 μM DDM (1× critical micelle concentration to prevent detergent exchange) and then overnight at 4 °C in 1 l CD buffer supplemented with 510 μM DDM. Samples were kept at 4 °C or on ice from this point forward. Protein concentration was determined against the final dialysis buffer using an absorbance at 280 nm and an extinction coefficient of 32,430 $M^{-}cm^{-}$ for the FtsLB complex (calculated *via* ExPASy). Protein was diluted to ∼14 μM, then filtered with 0.22 μm (diameter of 13 mm) polyvinyl difluoride syringe filters (CELLTREAT) before redetermining the final protein concentration. Samples were degassed in a vacuum chamber for at least 30 min and then centrifuged for 20 min at 21,000*g*. The final dialysis buffer was also filtered and degassed in the same manner to use as a blank in the CD experiments. CD spectra were obtained using an Aviv model 420 CD spectrometer and quartz cuvettes with a 0.1 cm path length. All spectra were recorded in 1 nm increments, with either a 10 s or a 20 s averaging time, and after a 5 min equilibration time upon reaching a 0.3 °C deadband. The spectra were baseline corrected by buffer subtraction. For the CD-monitored thermal melting experiments, the samples were heated at 3 °C intervals with a 20 s equilibration time. Because the transitions were not reversible, detailed thermodynamic analyses were not carried out, and the curves were only fitted to sigmoidal transitions to calculate their temperature midpoints (T_m).

Bioinformatics analysis

Homologs of FtsB and FtsL were collected using the DELTA-BLAST algorithm (57) on the RefSeq database (58). FtsB–FtsL pairs were selected by the National Center for

Biotechnology Information taxonomic identifier. In the case of multiple sequences per taxa, the one with the lowest E-value to the query *E. coli* FtsB or FtsL sequence was selected. Proteobacterial sequences were identified *via* the National Center for Biotechnology Information taxonomy database (59). Sequences were aligned using the MAFFT algorithm (60). Statistical analyses were performed in R software (61) with the aid of the following packages: tidyverse (62), tidymodels (63), Biostrings (64), zoo (65), taxize (66), rentrez (67), and tidygraph (68).

Molecular modeling

Modeling of the rearranged FtsLB complex was performed as described previously (29). Briefly, the FtsLB heterodimer was modeled using a Monte Carlo procedure to model supercoiled helical bundles (69). The superhelical radius (r_1), superhelical pitch (P), helical rotation (Φ_1), and z-shift (s) of both $FtsL_{52-94}$ and $FtsB_{21-63}$ were freely altered, whereas the rise per residue (h) and helical radius (r_0) were kept constant. Energies were calculated based on CHARMM 22 van der Waals and CHARMM 22 electrostatic terms with additional sigmoidal distance restraints for each pair of evolutionary couplings in the coiled-coil region (29). The heterodimeric FtsLB coiled coil was then aligned with one-half of the previously modeled heterotetrameric transmembrane domain using residues 52 to 58 of FtsL, which were present in both models. Both domains were kept parallel to the *Z*-axis. The juxtamembrane regions of FtsL and FtsB were then replaced with loops corresponding to fragments from the PDB. For FtsB, six-residue loops (corresponding to positions 21–26) with four flanking helical residues on each side were used, with an additional sequence requirement that the fragment contains at least one glycine. For FtsL, 15-residue fragments with four flanking helical residues on each side were used with the requirement that the loop has helical secondary structure. This arrangement was made C_2-symmetric to generate the Y-model. Finally, the side chains were repacked using a greedy trials algorithm, and the model was minimized using Broyden–Fletcher–Goldfarb–Shanno constrained optimization in CHARMM (70).

Protein structure prediction using AlphaFold2

The FtsLB complex was predicted with AlphaFold using the AlphaFold2_advanced notebook from Colabfold (70, 71), which allows for predictions of protein complexes. The full sequences of FtsB and FtsL were used as input, with two chains for each protein to model a 2:2 heterotetramer. Mmseqs2 (72) was chosen for multiple sequence alignment generation, and the use_turbo option was enabled.

All-atom MD simulations

For the MD simulations, the model's coiled-coil region was extended to avoid end effects to residues 110 (FtsL) and 79 (FtsB). The cytoplasmic side of FtsL was also extended to include residues 30 to 34, modeled in ideal α-helix. Three 400 ns all-atom MD simulations were performed using the CHARMM36m force field (73) and NAMD 2.10 software (74, 75). CHARMM-GUI membrane builder (76) was used to prepare systems composed of a 1-Palmitoyl-2-oleoyl-*sn*-glycero-3-phosphoethanolamine bilayer consisting of 301 lipids, the FtsLB tetramer, an ionic concentration of 0.150 M NaCl, and 59,163 TIP3P water molecules for hydration. The size of the boxes at the beginning of the simulation was approximately 97 × 97 × 242 $Å^3$. The simulations were initially minimized and equilibrated for 75 ps at an integration time of 1 fs/step and for 600 ps at an integration time of 2 fs/step. The integration time step for the production runs of each of the systems was 2.0 fs/step. The simulations were carried out in the NPT ensemble at a pressure of 1 atm and a temperature of 310.15 K, using the Nose–Hoover Langevin piston and Langevin dynamics method. Particle mesh Ewald method was used for electrostatic interactions, and a 12 Å cutoff was applied to Lennard–Jones interactions with a switching function from 10 to 12 Å. The RMSD analysis was performed using the RMSD trajectory tool in VMD (77). Hydrogen bonding analysis was performed with an in-house script.

Data availability

Bacterial strains and plasmids are available from the authors upon request (senes@wisc.edu). The Y-model and the AlphaFold2 model of FtsLB can be downloaded from http://seneslab.org or from the authors upon request. The molecular software libraries are available for download from https://sourceforge.net/projects/mslib/. Code is also available from the authors upon request.

Supporting information—This article contains supporting information (29, 30, 33, 47, 53).

Author contributions—S. J. C., S. G. F. C., and A. S. conceptualization; S. G. F. C. and G. D. V. software; S. J. C., S. G. F. C., G. D. V., and A. S. formal analysis; S. J. C., S. G. F. C., and G. D. V. investigation; S. J. C., S. G. F. C., and A. S. writing–original draft; G. D. V. and Q. C. writing–review & editing; Q. C. and A. S. supervision; Q. C. and A. S. funding acquisition.

Funding and additional information—This work was supported in part by the National Institutes of Health grant R01-GM099752 and R35-GM130339 (to A. S.) and National Science Foundation grant CHE-1829555 (to Q. C.). S. J. C. was supported in part by a Dr James Chieh-Hsia Mao Wisconsin Distinguished Fellowship. S. G. F. C. was supported in part by the Arthur B. Michael Departmental Fellowship and the William R. & Dorothy E. Sullivan Wisconsin Distinguished Graduate Fellowship. G. D. V. was supported in part by a SciMed GRS Fellowship. The content is solely the responsibility of the authors and does not necessarily represent the official views of the National Institutes of Health.

Conflict of interest—The authors declare that they have no conflicts of interest with the contents of this article.

Abbreviations—The abbreviations used are: AWI, activation of FtsWI; CCD, constriction control domain; DDM, *n*-dodecyl-β-D-maltopyranoside; MD, molecular dynamics; βME, β-mercaptoethanol; PDB, Protein Data Bank; PG, peptidoglycan.

References

1. Du, S., and Lutkenhaus, J. (2017) Assembly and activation of the Escherichia coli divisome. *Mol. Microbiol.* **105**, 177–187
2. den Blaauwen, T., Hamoen, L. W., and Levin, P. A. (2017) The divisome at 25: The road ahead. *Curr. Opin. Microbiol.* **36**, 85–94
3. Egan, A. J. F., Errington, J., and Vollmer, W. (2020) Regulation of peptidoglycan synthesis and remodelling. *Nat. Rev. Microbiol.* **18**, 446–460
4. Egan, A. J. F., and Vollmer, W. (2013) The physiology of bacterial cell division. *Ann. N. Y. Acad. Sci.* **1277**, 8–28
5. Booth, S., and Lewis, R. J. (2019) Structural basis for the coordination of cell division with the synthesis of the bacterial cell envelope. *Protein Sci. Publ. Protein Soc.* **28**, 2042–2054
6. Mercer, K. L. N., and Weiss, D. S. (2002) The Escherichia coli cell division protein FtsW is required to recruit its cognate transpeptidase, FtsI (PBP3), to the division site. *J. Bacteriol.* **184**, 904–912
7. Fraipont, C., Alexeeva, S., Wolf, B., van der Ploeg, R., Schloesser, M., den Blaauwen, T., and Nguyen-Distèche, M. (2011) The integral membrane FtsW protein and peptidoglycan synthase PBP3 form a subcomplex in Escherichia coli. *Microbiol. Read. Engl.* **157**, 251–259
8. Cho, H., Wivagg, C. N., Kapoor, M., Barry, Z., Rohs, P. D. A., Suh, H., Marto, J. A., Garner, E. C., and Bernhardt, T. G. (2016) Bacterial cell wall biogenesis is mediated by SEDS and PBP polymerase families functioning semi-autonomously. *Nat. Microbiol.* **1**, 16172
9. Meeske, A. J., Riley, E. P., Robins, W. P., Uehara, T., Mekalanos, J. J., Kahne, D., Walker, S., Kruse, A. C., Bernhardt, T. G., and Rudner, D. Z. (2016) SEDS proteins are a widespread family of bacterial cell wall polymerases. *Nature* **537**, 634–638
10. Taguchi, A., Welsh, M. A., Marmont, L. S., Lee, W., Sjodt, M., Kruse, A. C., Kahne, D., Bernhardt, T. G., and Walker, S. (2019) FtsW is a peptidoglycan polymerase that is functional only in complex with its cognate penicillin-binding protein. *Nat. Microbiol.* **4**, 587–594
11. Mohammadi, T., van Dam, V., Sijbrandi, R., Vernet, T., Zapun, A., Bouhss, A., Diepeveen-de Bruin, M., Nguyen-Distèche, M., de Kruijff, B., and Breukink, E. (2011) Identification of FtsW as a transporter of lipid-linked cell wall precursors across the membrane. *EMBO J.* **30**, 1425–1432
12. Mohammadi, T., Sijbrandi, R., Lutters, M., Verheul, J., Martin, N. I., den Blaauwen, T., de Kruijff, B., and Breukink, E. (2014) Specificity of the transport of lipid II by FtsW in Escherichia coli. *J. Biol. Chem.* **289**, 14707–14718
13. Leclercq, S., Derouaux, A., Olatunji, S., Fraipont, C., Egan, A. J. F., Vollmer, W., Breukink, E., and Terrak, M. (2017) Interplay between Penicillin-binding proteins and SEDS proteins promotes bacterial cell wall synthesis. *Sci. Rep.* **7**, 43306
14. Botta, G. A., and Park, J. T. (1981) Evidence for involvement of penicillin-binding protein 3 in murein synthesis during septation but not during cell elongation. *J. Bacteriol.* **145**, 333–340
15. Nakagawà, J., Tamaki, S., and Matsuhashi, M. (1979) Purified penicillin binding proteins 1Bs from *Escherichia coli* membrane showing activities of both peptidoglycan polymerase and peptidoglycan crosslinking enzyme. *Agric. Biol. Chem.* **43**, 1379–1380
16. Yang, X., McQuillen, R., Lyu, Z., Phillips-Mason, P., De La Cruz, A., McCausland, J. W., Liang, H., DeMeester, K. E., Santiago, C. C., Grimes, C. L., de Boer, P., and Xiao, J. (2021) A two-track model for the spatio-temporal coordination of bacterial septal cell wall synthesis revealed by single-molecule imaging of FtsW. *Nat. Microbiol.* **6**, 584–593
17. McCausland, J. W., Yang, X., Squyres, G. R., Lyu, Z., Bruce, K. E., Lamanna, M. M., Söderström, B., Garner, E. C., Winkler, M. E., Xiao, J., and Liu, J. (2021) Treadmilling FtsZ polymers drive the directional movement of sPG-synthesis enzymes via a Brownian ratchet mechanism. *Nat. Commun.* **12**, 609
18. Gerding, M. A., Liu, B., Bendezú, F. O., Hale, C. A., Bernhardt, T. G., and de Boer, P. A. J. (2009) Self-enhanced accumulation of FtsN at division sites and roles for other proteins with a SPOR domain (DamX, DedD, and RlpA) in Escherichia coli cell constriction. *J. Bacteriol.* **191**, 7383–7401
19. Ursinus, A., van den Ent, F., Brechtel, S., de Pedro, M., Höltje, J.-V., Löwe, J., and Vollmer, W. (2004) Murein (peptidoglycan) binding property of the essential cell division protein FtsN from Escherichia coli. *J. Bacteriol.* **186**, 6728–6737
20. Yang, J.-C., Van Den Ent, F., Neuhaus, D., Brevier, J., and Löwe, J. (2004) Solution structure and domain architecture of the divisome protein FtsN. *Mol. Microbiol.* **52**, 651–660
21. Liu, B., Persons, L., Lee, L., and de Boer, P. A. J. (2015) Roles for both FtsA and the FtsBLQ subcomplex in FtsN-stimulated cell constriction in Escherichia coli. *Mol. Microbiol.* **95**, 945–970
22. Pichoff, S., Du, S., and Lutkenhaus, J. (2015) The bypass of ZipA by overexpression of FtsN requires a previously unknown conserved FtsN motif essential for FtsA-FtsN interaction supporting a model in which FtsA monomers recruit late cell division proteins to the Z ring. *Mol. Microbiol.* **95**, 971–987
23. Park, K.-T., Pichoff, S., Du, S., and Lutkenhaus, J. (2021) FtsA acts through FtsW to promote cell wall synthesis during cell division in Escherichia coli. *Proc. Natl. Acad. Sci. U. S. A.* **118,** e2107210118
24. Tsang, M.-J., and Bernhardt, T. G. (2015) A role for the FtsQLB complex in cytokinetic ring activation revealed by an ftsL allele that accelerates division. *Mol. Microbiol.* **95**, 925–944
25. Marmont, L. S., and Bernhardt, T. G. (2020) A conserved subcomplex within the bacterial cytokinetic ring activates cell wall synthesis by the FtsW-FtsI synthase. *Proc. Natl. Acad. Sci.* **117**, 23879–23885
26. Park, K.-T., Du, S., and Lutkenhaus, J. (2020) Essential role for FtsL in activation of septal peptidoglycan synthesis. *mBio* **11**, e03012–e03020
27. Li, Y., Gong, H., Zhan, R., Ouyang, S., Park, K.-T., Lutkenhaus, J., and Du, S. (2021) Genetic analysis of the septal peptidoglycan synthase FtsWI complex supports a conserved activation mechanism for SEDS-bPBP complexes. *PLoS Genet.* **17**, e1009366
28. Khadria, A. S., and Senes, A. (2013) The transmembrane domains of the bacterial cell division proteins FtsB and FtsL form a stable high-order oligomer. *Biochemistry* **52**, 7542–7550
29. Condon, S. G. F., Mahbuba, D.-A., Armstrong, C. R., Diaz-Vazquez, G., Craven, S. J., LaPointe, L. M., Khadria, A. S., Chadda, R., Crooks, J. A., Rangarajan, N., Weibel, D. B., Hoskins, A. A., Robertson, J. L., Cui, Q., and Senes, A. (2018) The FtsLB subcomplex of the bacterial divisome is a tetramer with an uninterrupted FtsL helix linking the transmembrane and periplasmic regions. *J. Biol. Chem.* **293**, 1623–1641
30. Gonzalez, M. D., Akbay, E. A., Boyd, D., and Beckwith, J. (2010) Multiple interaction domains in FtsL, a protein component of the widely conserved bacterial FtsLBQ cell division complex. *J. Bacteriol.* **192**, 2757–2768
31. Ghigo, J. M., Weiss, D. S., Chen, J. C., Yarrow, J. C., and Beckwith, J. (1999) Localization of FtsL to the Escherichia coli septal ring. *Mol. Microbiol.* **31**, 725–737
32. Ghigo, J. M., and Beckwith, J. (2000) Cell division in Escherichia coli: Role of FtsL domains in septal localization, function, and oligomerization. *J. Bacteriol.* **182**, 116–129
33. Goehring, N. W., Gonzalez, M. D., and Beckwith, J. (2006) Premature targeting of cell division proteins to midcell reveals hierarchies of protein interactions involved in divisome assembly. *Mol. Microbiol.* **61**, 33–45
34. Choi, Y., Kim, J., Yoon, H.-J., Jin, K. S., Ryu, S., and Lee, H. H. (2018) Structural insights into the FtsQ/FtsB/FtsL complex, a key component of the divisome. *Sci. Rep.* **8**, 18061
35. Kureisaite-Ciziene, D., Varadajan, A., McLaughlin, S. H., Glas, M., Montón Silva, A., Luirink, R., Mueller, C., den Blaauwen, T., Grossmann, T. N., Luirink, J., and Löwe, J. (2018) Structural analysis of the interaction between the bacterial cell division proteins FtsQ and FtsB. *mBio* **9**, e01346–18
36. LaPointe, L. M., Taylor, K. C., Subramaniam, S., Khadria, A., Rayment, I., and Senes, A. (2013) Structural organization of FtsB, a transmembrane protein of the bacterial divisome. *Biochemistry* **52**, 2574–2585
37. Villanelo, F., Ordenes, A., Brunet, J., Lagos, R., and Monasterio, O. (2011) A model for the Escherichia coli FtsB/FtsL/FtsQ cell division complex. *BMC Struct. Biol.* **11**, 28

38. Buddelmeijer, N., and Beckwith, J. (2004) A complex of the Escherichia coli cell division proteins FtsL, FtsB and FtsQ forms independently of its localization to the septal region. *Mol. Microbiol.* **52**, 1315–1327
39. Masson, S., Kern, T., Le Gouëllec, A., Giustini, C., Simorre, J.-P., Callow, P., Vernet, T., Gabel, F., and Zapun, A. (2009) Central domain of DivIB caps the C-terminal regions of the FtsL/DivIC coiled-coil rod. *J. Biol. Chem.* **284**, 27687–27700
40. Woolfson, D. N. (2005) The design of coiled-coil structures and assemblies. *Adv. Protein Chem.* **70**, 79–112
41. Harbury, P. B., Zhang, T., Kim, P. S., and Alber, T. (1993) A switch between two-, three-, and four-stranded coiled coils in GCN4 leucine zipper mutants. *Science* **262**, 1401–1407
42. Gonzalez, L., Woolfson, D. N., and Alber, T. (1996) Buried polar residues and structural specificity in the GCN4 leucine zipper. *Nat. Struct. Biol.* **3**, 1011–1018
43. Wagschal, K., Tripet, B., Lavigne, P., Mant, C., and Hodges, R. S. (1999) The role of position a in determining the stability and oligomerization state of alpha-helical coiled coils: 20 amino acid stability coefficients in the hydrophobic core of proteins. *Protein Sci. Publ. Protein Soc.* **8**, 2312–2329
44. Testa, O. D., Moutevelis, E., and Woolfson, D. N. (2009) CC+: A relational database of coiled-coil structures. *Nucleic Acids Res.* **37**, D315–D322
45. Jumper, J., Evans, R., Pritzel, A., Green, T., Figurnov, M., Ronneberger, O., Tunyasuvunakool, K., Bates, R., Žídek, A., Potapenko, A., Bridgland, A., Meyer, C., Kohl, S. A. A., Ballard, A. J., Cowie, A., *et al.* (2021) Highly accurate protein structure prediction with AlphaFold. *Nature* **596**, 583–589
46. Glas, M., van den Berg van Saparoea, H. B., McLaughlin, S. H., Roseboom, W., Liu, F., Koningstein, G. M., Fish, A., den Blaauwen, T., Heck, A. J. R., de Jong, L., Bitter, W., de Esch, I. J. P., and Luirink, J. (2015) The soluble periplasmic domains of Escherichia coli cell division proteins FtsQ/FtsB/FtsL form a trimeric complex with submicromolar affinity. *J. Biol. Chem.* **290**, 21498–21509
47. Gonzalez, M. D., and Beckwith, J. (2009) Divisome under construction: Distinct domains of the small membrane protein FtsB are necessary for interaction with multiple cell division proteins. *J. Bacteriol.* **191**, 2815–2825
48. Schmidt, N. W., Grigoryan, G., and DeGrado, W. F. (2017) The accommodation index measures the perturbation associated with insertions and deletions in coiled-coils: Application to understand signaling in histidine kinases. *Protein Sci. Publ. Protein Soc.* **26**, 414–435
49. Bhate, M. P., Lemmin, T., Kuenze, G., Mensa, B., Ganguly, S., Peters, J. M., Schmidt, N., Pelton, J. G., Gross, C. A., Meiler, J., and DeGrado, W. F. (2018) Structure and function of the transmembrane domain of NsaS, an antibiotic sensing histidine kinase in Staphylococcus aureus. *J. Am. Chem. Soc.* **140**, 7471–7485
50. Albanesi, D., Martín, M., Trajtenberg, F., Mansilla, M. C., Haouz, A., Alzari, P. M., de Mendoza, D., and Buschiazzo, A. (2009) Structural plasticity and catalysis regulation of a thermosensor histidine kinase. *Proc. Natl. Acad. Sci. U. S. A.* **106**, 16185–16190
51. Fernández, P., Porrini, L., Albanesi, D., Abriata, L. A., Dal Peraro, M., de Mendoza, D., and Mansilla, M. C. (2019) Transmembrane Prolines mediate signal sensing and Decoding in Bacillus subtilis DesK histidine kinase. *mBio* **10**, e02564–19
52. Lesne, E., Krammer, E.-M., Dupre, E., Locht, C., Lensink, M. F., Antoine, R., and Jacob-Dubuisson, F. (2016) Balance between coiled-coil stability and dynamics regulates activity of BvgS sensor kinase in Bordetella. *mBio* **7**, e02089
53. Buddelmeijer, N., Judson, N., Boyd, D., Mekalanos, J. J., and Beckwith, J. (2002) YgbQ, a cell division protein in Escherichia coli and Vibrio cholerae, localizes in codependent fashion with FtsL to the division site. *Proc. Natl. Acad. Sci. U. S. A.* **99**, 6316–6321
54. Paintdakhi, A., Parry, B., Campos, M., Irnov, I., Elf, J., Surovtsev, I., and Jacobs-Wagner, C. (2016) Oufti: An integrated software package for high-accuracy, high-throughput quantitative microscopy analysis. *Mol. Microbiol.* **99**, 767–777
55. Efron, B. (1979) Bootstrap methods: Another look at the Jackknife. *Ann. Stat.* **7**, 1–26
56. Studier, F. W. (2005) Protein production by auto-induction in high density shaking cultures. *Protein Expr. Purif.* **41**, 207–234
57. Boratyn, G. M., Schäffer, A. A., Agarwala, R., Altschul, S. F., Lipman, D. J., and Madden, T. L. (2012) Domain enhanced lookup time accelerated BLAST. *Biol. Direct* **7**, 12
58. O'Leary, N. A., Wright, M. W., Brister, J. R., Ciufo, S., Haddad, D., McVeigh, R., Rajput, B., Robbertse, B., Smith-White, B., Ako-Adjei, D., Astashyn, A., Badretdin, A., Bao, Y., Blinkova, O., Brover, V., *et al.* (2016) Reference sequence (RefSeq) database at NCBI: Current status, taxonomic expansion, and functional annotation. *Nucleic Acids Res.* **44**, D733–D745
59. Federhen, S. (2012) The NCBI taxonomy database. *Nucleic Acids Res.* **40**, D136–D143
60. Katoh, K., and Standley, D. M. (2013) MAFFT multiple sequence alignment software version 7: Improvements in performance and usability. *Mol. Biol. Evol.* **30**, 772–780
61. R Core Team (2019) *R: A Language and Environment for Statistical Computing*, R Foundation for Statistical Computing, Vienna, Austria
62. Wickham, H., Averick, M., Bryan, J., Chang, W., D'Agostino McGowan, L., François, R., Grolemund, G., Hayes, A., Henry, L., Hester, J., Kuhn, M., Pedersen, T. L., Miller, E., Bache, S. M., Müller, K., *et al.* (2019) Welcome to the tidyverse. *J. Open Source Soft* **4**, 1686
63. Kuhn, M., and Wickham, H. (2020) *Tidymodels: A Collection of Packages for Modeling and Machine Learning Using Tidyverse Principles*
64. Pagès, H., Aboyoun, P., Gentleman, R., and DebRoy, S. (2019) *Biostrings: Efficient Manipulation of Biological Strings*
65. Zeileis, A., and Grothendieck, G. (2005) Zoo: S3 infrastructure for regular and irregular time series. *J. Stat. Softw.* **14**, 1–27
66. Chamberlain, S., and Szocs, E. (2013) *taxize - taxonomic search and retrieval in R, F1000Research* **2**, 191
67. Winter, D. J. (2017) rentrez: an R package for the NCBI eUtils API. *R. J.* **9**, 520–526
68. Pedersen, T. L. (2019) *Tidygraph: A Tidy API for Graph Manipulation*
69. Grigoryan, G., and DeGrado, W. F. (2011) Probing designability via a generalized model of helical bundle geometry. *J. Mol. Biol.* **405**, 1079–1100
70. Brooks, B. R., Bruccoleri, R. E., Olafson, B. D., States, D. J., Swaminathan, S., and Karplus, M. (1983) Charmm: A program for macromolecular energy, minimization, and dynamics calculations. *J. Comput. Chem.* **4**, 187–217
71. [preprint] Mirdita, M., Ovchinnikov, S., and Steinegger, M. (2021) ColabFold - Making protein folding accessible to all. *Bioinformatics*
72. Steinegger, M., and Söding, J. (2017) MMseqs2 enables sensitive protein sequence searching for the analysis of massive data sets. *Nat. Biotechnol.* **35**, 1026–1028
73. Huang, J., Rauscher, S., Nawrocki, G., Ran, T., Feig, M., de Groot, B. L., Grubmüller, H., and MacKerell, A. D. (2017) CHARMM36m: An improved force field for folded and intrinsically disordered proteins. *Nat. Methods* **14**, 71–73
74. Klauda, J. B., Venable, R. M., Freites, J. A., O'Connor, J. W., Tobias, D. J., Mondragon-Ramirez, C., Vorobyov, I., MacKerell, A. D., and Pastor, R. W. (2010) Update of the CHARMM all-atom additive force field for lipids: Validation on six lipid types. *J. Phys. Chem. B* **114**, 7830–7843
75. Phillips, J. C., Braun, R., Wang, W., Gumbart, J., Tajkhorshid, E., Villa, E., Chipot, C., Skeel, R. D., Kalé, L., and Schulten, K. (2005) Scalable molecular dynamics with NAMD. *J. Comput. Chem.* **26**, 1781–1802
76. Jo, S., Kim, T., Iyer, V. G., and Im, W. (2008) CHARMM-GUI: A web-based graphical user interface for CHARMM. *J. Comput. Chem.* **29**, 1859–1865
77. Humphrey, W., Dalke, A., and Schulten, K. (1996) Vmd: Visual molecular dynamics. *J. Mol. Graph.* **14**, 27–28